Rapid biomimetic mineralization of collagen fibrils and combining with human umbilical cord mesenchymal stem cells for bone defects healing

Bihua Ye [a], Xueshi Luo [a], Zhiwen Li [a], Caiping Zhuang [b], Lihua Li [a,*], Lu Lu [a], Shan Ding [a], Jinhuan Tian [a], Changren Zhou [a,*]

[a] Department of Material Science and Engineering, Engineering Research Center of Artificial Organs and Materials, Jinan University, Guangzhou 510632, China
[b] Department of Anesthesiology, Huizhou Central People's Hospital, Huizhou 516001, China

ARTICLE INFO

ABSTRACT

Collagen biomineralization is regulated by complicated interactions between the collagen matrix and non-collagenous extracellular proteins. Here, the use of sodium tripolyphosphate to simulate the templating functional motif of the C-terminal fragment of non-collagenous proteins is reported, and a low molecular weight polyacrylic acid served as a sequestration agent to stabilize amorphous calcium phosphate into nanoprecursors. Self-assembled collagen fibrils served as a fixed template for achieving rapid biomimetic mineralization in vitro. Results demonstrated that, during the mineralization process, intrafibrillar and extrafibrillar hydroxyapatite mineral with collagen fibrils formed and did so via bottom-up nanoparticle assembly based on the non-classical crystallization approach in the presence of these dual biomimetic functional analogues. In vitro human umbilical cord mesenchymal stem cell (hUCMSC) culture found that the mineralized scaffolds have a better cytocompatibility in terms of cell viability, adhesion, proliferation, and differentiation into osteoblasts. A rabbit femoral condyle defect model was established to confirm the ability of the n-HA/collagen scaffolds to facilitate bone regeneration and repair. The images of gross anatomy, MRI, CT and histomorphology taken 6 and 12 weeks after surgery showed that the biomimetic mineralized collagen scaffolds with hUCMSCs can promote the healing speed of bone defects in vivo, and both of the scaffolds groups performing better than the bone defect control group. As new bone tissue formed, the scaffolds degraded and were gradually absorbed. All these results demonstrated that both of the scaffolds and cells have better histocompatibility.

© 2016 Elsevier B.V. All rights reserved.

1. Introduction

Collagen, the primary structural protein in connective tissues, can self-assemble into fibrils and interweave itself into insoluble networks of fibrous bundles for scaffolding to offer shape and support in vivo [1–3]. Moreover, as the main component of bone tissues, the type I collagen has been proven to play an important role in the control and templating of hydroxyapatite (HA) formation during biomineralization [4–7]. Collagen biomineralization is regulated by complicated interactions among the collagen matrix, non-collagenous extracellular proteins, and calcium phosphate mineral. Currently, certain non-collagenous proteins (NCPs) such as dentine matrix protein (DMP1), dentine phosphophoryn (DPP), and bone sialoprotein (BSP), are believed to regulate nucleation, orientation, and the hierarchy of apatite during biomineralization for obtaining hierarchical structures in organic-inorganic nanocomposites [8–10]. Specifically, such non-collagenous proteins can not only stabilize amorphous calcium phosphate (ACP) into nanoprecursors (sequestration motif) but can also initiate nucleation and hierarchical assembly of apatite within the collagen fibrils (templating motif) [11,12]. These proteins contribute to the intrafibrillar and extrafibrillar mineralization of collagen fibrils considerably. However, their limited availability and high cost of production hinder their applications in bone tissue engineering.

Stem cells-based tissue engineering has great potential to regenerate damaged and diseased tissues. Human umbilical cord mesenchymal stem cells (hUCMSCs) are a relatively new source of cells, and they have been shown to differentiate into osteoblasts, chondrocytes, neurons, endothelial cells, and other cells [13,14]. Umbilical cords can provide an inexhaustible, low-cost supply of stem cells, and they require no invasive procedures to harvest. Furthermore, hUCMSCs appeared to be primitive MSCs and exhibited a high plasticity and developmental flexibility. In addition, in preliminary studies the hUCMSCs had minimal immunorejection in vivo and were not tumorigenic [15,16]. Diao et al. fabricated a HA/collagen/poly-L-lactide acid composite scaffold with UCMSCs, which showed successful in vivo osteogenesis [17]. In another study, after hUCMSCs that had been mixed with the HA/tricalcium phosphate (TCP) composite were implanted into the subcutaneous region of immuno-deficient mice for 8 weeks, ectopic bone formation was observed on the surface of the HA/TCP composite material [18].

* Corresponding authors.
E-mail addresses: tlihuali@jnu.edu.cn (L. Li), tcrz9@jnu.edu.cn (C. Zhou).

In order to mimic the components and structure of natural bones, a rapid biomimetic mineralization approach was established to provide a three-dimensional porous and heavily mineralized hydroxyapatite/collagen composite scaffold for bone regeneration. A-low-molecular weight polyacrylic acid (PAA) was used to imitate the sequestration functional motif of the N-terminal fragment cleaved from the acidic NCPs, for stabilizing ACPs into nanoprecursors. On the other hand, sodium tripolyphosphate (TPP), a small inorganic polyphosphate, was used to simulate the templating functional motif of the C-terminal fragment cleaved from the acidic NCPs, attracting ACPs for initiating nucleation and then templating the hierarchical assembly of them within the collagen fibrils. During biomimetic mineralization, both templates appeared to be dynamic, while the self-assembled collagen fibrils served as a fixed template. The possibility of the universal application of hUCMSCs in bone regeneration must be evaluated. n-HA/COL scaffolds with and without hUCMSCs were compared with respect to the critical size of femoral condyle defects to assess healing, wherein hUCMSCs were obtained from more than one single cord, and immune rabbits were used instead of minimally immune rats.

2. Materials and methods

2.1. Materials

Type I collagen from pigskin was purchased from Sichuan Mingrang Bio-tech Co., Ltd. (China). Sodium tripolyphosphate (TPP), polyacrylic acid (PAA, Mw 1800 Da), and sodium β-glycerophosphate (β-GP) were purchased from Sigma-Aldrich (U.S.). $CaCl_2$ was purchased from Guangzhou Chemical Reagent Factory (China). High-glucose Dulbecco's modified Eagle's medium (DMEM) and fetal bovine serum (FBS) were purchased from Hyclone Inc. (U.S.), and 0.25% trypsin-EDTA was from Gibco-BRL (Grand Island, U.S.). All other reagents were of analytical grade and used without further purification.

2.2. Preparation of n-HA/collagen composite scaffolds regulated by dual biomimetic analogues

The specific preparation process of the n-HA/collagen composite scaffolds is shown in Fig. 1. The type I collagen powder derived from pigskin was dissolved in 10 mM HCl to form a homogeneous solution, and then 96 mmol $CaCl_2$ powder was added slowly. After the powder was completely dissolved, the collagen-$CaCl_2$ solution was stirred in ammonia atmosphere for neutralization. With the same volume of 10 mM HCl, 25 mM Tris-HCl buffer solution was divided into two equal portions: TPP powder was added to and PAA and β-GP powder was added to the other. Then the TPP Tris-HCl solution was dropped into the collagen-$CaCl_2$ solution under magnetic stirring. After stirring for 5–10 min, PAA-(β-GP) Tris-HCl solution was dropped into the collagen-$CaCl_2$-TPP solution under magnetic stirring to form a biomimetic mineralization solution, and the final concentration of each component in the solution was 5 mg/mL collagen, 48 mM $CaCl_2$, 28.8 mM β-GP, 0.5% (wt%) TPP and 1 mg/mL PAA. The reaction mixtures were incubated for 0.5 h–24 h at 37 °C. Finally, after more than three rinses in tri-distilled water, the mixtures were kept at −80 °C for 24 h and were then freeze-dried. The nano-HA/collagen composite scaffolds (named as n-HA/COL) were produced in this way, regulated by TPP and PAA as biomimetic analogues (templating and sequestration analogues control).

The aforementioned experiments were repeated to prepare the collagen negative control (no templating or sequestration of analogue controls), the templating analogue control (no PAA) and the sequestration analogue control (no TPP).

2.3. Characterization of the composite scaffolds

The results of Fourier transform infrared spectroscopy (FTIR) measurement were determined using an EQUINOX55 spectrometer (Bruker, Germany) equipped with an attenuated total reflectance (ATR) accessory. Infrared spectra were collected between 600 and 4000 cm^{-1} at 4 cm^{-1} resolution using 32 scans with atmospheric water and carbon dioxide corrections.

X-ray diffraction (XRD) patterns were assessed using a powder X-ray diffractometer (MSAL XD-2, Beijing Purkinje General Instrument Co. Ltd., China) using Cu Kα radiation (40 kV, 20 mA, λ = 1.54051 Å), in the 2θ range of 10–60°, with the scan rate of 4°/min and a sampling interval of 0.02°.

The freeze-dried samples were carefully fractured and sputter-coated with gold for morphological observation with a field emission scanning electron microscope (FESEM, Nova NanoSEM430, FEI, The Netherlands) at 3.0–5.0 kV.

Epoxy resin-embedded ultrathin sections (90 nm thick) were prepared using an Ultramicrotome (EM UC6, Leica, Germany) and examined without further staining with a high-resolution transmission
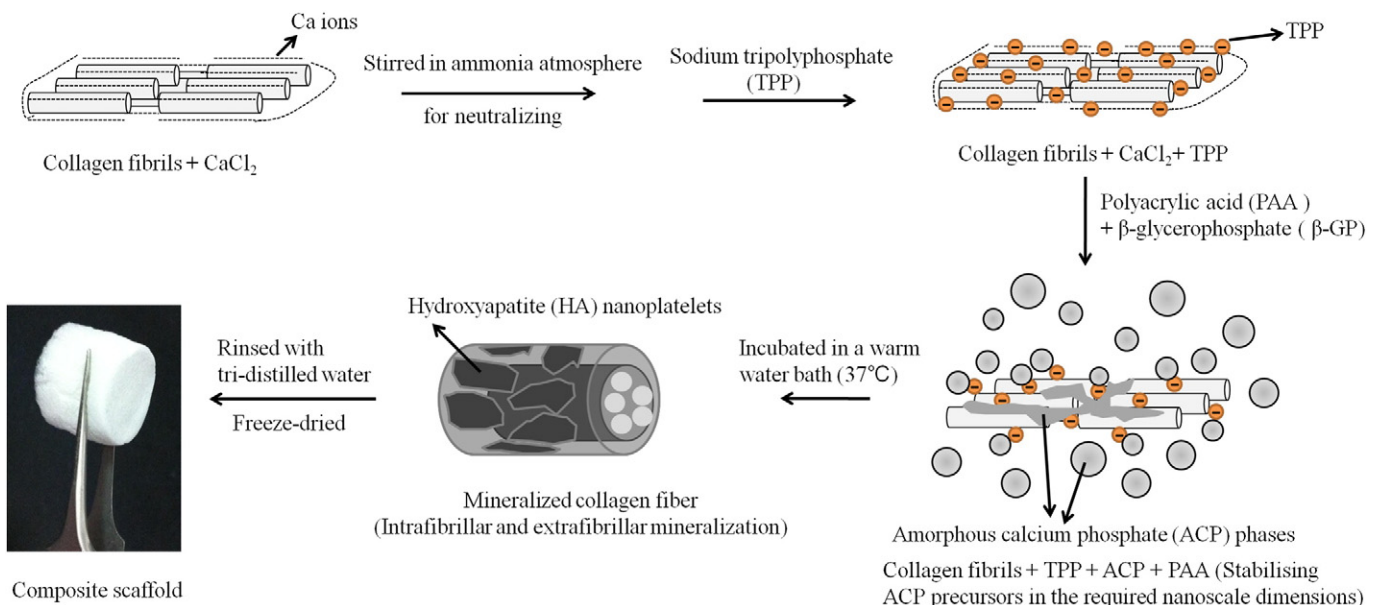

Fig. 1. Specific processes in the preparation of n-HA/collagen composite scaffolds regulated by dual biomimetic analogues.

electron microscope (HRTEM, JEM-2100F, JEOL, Japan) and selected area electron diffraction (SAED) at 100 kV.

The freeze-dried n-HA/COL scaffolds were loaded in unconfined uniaxial compression at a displacement rate of 1.0 mm/min to ~75% strain using an electronic universal testing machine (AG-1, SHIMADZU, Japan). The compressive modulus was measured from the stress-strain curve by linear regression from the slopes in the initial elastic region and the compressive strength was defined as the result of 60% strain.

The porosity of the n-HA/COL scaffolds were measured by liquid displacement method [19]. Specifically, the sample was immersed into a known volume of dehydrated alcohol (V_1) for 4 h until it was saturated by absorbing the alcohol. Then, the total volume of alcohol and alcohol-impregnated scaffold was recorded (V_2). After the alcohol-impregnated scaffold was removed, the residual alcohol volume was recorded (V_3). Each sample was measured in triplicate. The porosity of the scaffolds was calculated using the equation: Porosity = $[(V_1 - V_3) / (V_2 - V_3)] \times 100\%$.

2.4. Cell culture

The original hUCMSCs were obtained from the umbilical cord of healthy babies born by normal-term delivery in the Guangzhou Overseas Chinese hospital, and isolated as previously described [20]. The use of hUCMSCs for this study was approved by Jinan University and maternal consent was obtained. HUCMSCs were cultured in high-glucose DMEM with 10% FBS and 1% penicillin/streptomycin. They were then seeded in plastic tissue culture flasks at 6000 cells/cm^2 (passage 1). Thereafter, the cells were incubated in a humidified atmosphere of 5% CO$_2$ with nutrient medium at 37 °C and the culture medium was changed every other day. Until reaching 80–90% confluence, the cells were detached by 0.25% trypsin and passaged at 6000 cells/cm^2. Passage 5 hUCMSCs were used for the following experiments.

n-HA/COL composites with dual biomimetic analogues treatment aged 24 h were selected for cell culture. After sterilization with ^{60}Co (5 kGy), the composites (Ø10 mm × 8 mm) were rinsed three times with phosphate buffered saline (PBS) and then transferred into 6-well culture plates (Costar, Corning Life Sciences B.V., Amsterdam, The Netherlands) with cell culture medium overnight. A seeding density of 4×10^5 cells was added drop-wise into each well and incubated for 5 h in a humidified atmosphere of 5% CO$_2$ at 37 °C. Then all the wells were transferred to new culture plates and supplied with sufficient cell culture medium. Four groups were investigated. Group A: hUCMSCs without scaffolds. Group B: hUCMSCs without scaffolds but with osteoblast-inducing conditional media (OICM). Group C: hUCMSCs with scaffolds. Group D: hUCMSCs with scaffolds and OICM. The medium was renewed twice each week.

2.5. Cell adhesion

Cells in the old medium and those that adhered to the wells of the old cell culture plates were collected and counted using a hemocytometer. The number of cells in each well was considered the number of unattached cells. The difference between the number of unattached cells and the number of seeded cells could be considered the number of cells attached to the scaffold. The cell seeding efficiency of each sample could also be quantified by dividing the number of attached cells by the number of seeded cells [21]. Specifically, the cell adherence ratio of the samples was calculated using the equation $[(N_s - N_u) / N_s] \times 100\%$, where N_s is the number of seeded cells and N_u is the number of unattached cells.

2.6. Analysis of cell morphology, ECM distribution, and biochemical assays

After seven days of culture, the morphology of hUCMSCs and the distribution of ECM in the samples were observed via inverted microscope and SEM.

The cell/scaffold constructs were transferred into other culture plates, washed three times with PBS (10 min/rinse), and fixed with 2.5% glutaraldehyde (GA) solution at room temperature for 4 h. The fixed cell/scaffold constructs were then washed three times with PBS (10 min/rinse) and gradient dehydration by ethanol. After freeze-drying, the samples were sputter-coated with gold for SEM observation.

2.7. Determination of the ALP activity

The differentiation of cells was analyzed with alkaline phosphatase (ALP) enzyme activity after 7, 14, and 21 days. The cell/scaffold constructs were broken into small pieces, rinsed with PBS, and air-dried for 10 min. Then those pieces were lysed using with 0.1% Triton X-100 for 30 min, and the lysates were then centrifuged at 13,000 rpm for 5 min at 4 °C. The ALP activity in the supernatant was analyzed using the ALP kit (Jian cheng, Nanjing, China) and the mixture was incubated at 37 °C. The absorbance of these samples was measured at 405 nm at 37 °C via the ultraviolet-visible spectrophotometer. The data were analyzed using the SPSS 16.0 (SPSS, Chicago, IL, U.S.) analysis software and expressed as mean ± SD. $P \leq 0.05$ was considered statistically significant.

2.8. In vivo animal experiment

The animal experiments were performed in compliance with the Animal Welfare Act and approved by the Institutional Animal Care and Use Committee of the Laboratory Animal Research Centre at Jinan University. Three groups were tested for the in vivo femur repair model: hUCMSC-seeded n-HA/COL scaffolds (group A), n-HA/COL scaffolds (group B), and a blank control without scaffolds. The hUCMSC-seeded scaffolds were cultured in OICM for 14 days and then used for implantation. Here, 36 New Zealand rabbits (2.1–3.0 kg, 6 weeks old) were anesthetized by intraperitoneal injection with a combination of 30-mg/kg body weight of 2% pentobarbital sodium and 10 mg/kg of xylazine. A 3.0 cm longitudinal skin incision was made over the bilateral distal medial femurs. Surgery was performed under aseptic conditions. The femur was exposed, and a critical-sized circular bone defect with a diameter of Ø8 mm × 6 mm was drilled close to femoral condyle bone. Afterwards, the wound was carefully washed with normal saline to remove any bone debris from the defect, which was a crucial step in this procedure of evaluating the formation of new bone within the defect as previously described [22]. Finally, the samples were placed in the defect and the defect was closed by suturing the soft tissue. Two implantation periods were tested: 6 and 12 weeks.

2.9. Medical imaging examination

Before histological analyses, pre-contrast magnetic resonance imaging (MRI, GE, U.S.) and micro-CT (Toshiba, Japan) analysis were performed. Three rabbits were randomly selected from each group and anesthetized. The bone defects, surrounding tissue inflammation, tissue edema, and bone regeneration were observed. Rabbits were then euthanized and checked for purulent infection, defects, and accidental fractures. Finally, the upper femurs were amputated and the specimens were removed intact and photographed.

2.10. Histological and morphological analysis

After removing soft tissues, femurs were isolated and fixed by gradient ethanol to dehydrate for 14 days, embedded in 10% formaldehyde solution for 48 h, and then decalcified in 10% EDTA-Na in an incubator at 37 °C. After dehydration and clearing, the specimens were embedded in paraffin and the central part of the implant and defect was cut into 5 μm thick sections. Paraffin sections were stained with hematoxylin/eosin (H&E).

3. Results and discussion

3.1. The composition of the collagen matrix

Infrared spectra of reconstituted collagen, synthetic hydroxyapatite and n-HA/collagen composite scaffolds with different aging treatment are shown in Fig. 2. Before TPP and PAA treatment, the type I collagen revealed characteristic amide I, II and III bands at about 1639, 1548 and 1237 cm^{-1}, respectively. After regulating using TPP and PAA as functional analogues of matrix phosphoproteins, new absorption peaks that were attributed to vibrations in the ν_3 asymmetric and ν_1 symmetric stretching modes of the phosphate groups could be identified at 1096, 980, and 897 cm^{-1} [11,23]. The intensities of the peaks were found to be related to collagen bands between amide II and amide III, and both decreased simultaneously, which was attributed to the wagging vibrations of the glycine backbone and proline side chains [24]. Besides, when compared to the baseline collagen spectrum, the amide I band peak that corresponded to the C=O stretch vibration decreased in intensity as incubation continued, which indicated that the C=O bonds were weakened by the chelation of Ca^{2+} and C=O bonds [25]. This also indicated that the carbonyl groups on the surface of collagen fibrils could attract Ca^{2+} via electrostatic interaction, working as a kind of calcium phosphate nucleation sites to initiate nucleation.

3.2. Inorganic phase analysis of the composite scaffolds

The XRD patterns of different control groups after treatment for 0.5 h at 37 °C and commercially purchased HA powders are shown in Fig. 3. The calcium phosphate nanocrystals were obtained in a very short time by this method. When compared to the XRD pattern of commercial HA products (Fig. 3a), no differences in the diffraction peak positions of each control group (Fig. 3b, c, d, and e) were observed, which indicated that whether biomimetic analogues were present or not, the inorganic phase in each control group was substantially the same (i.e. HA analogues). This indication suggested that collagen played a predominant role in controlling and templating apatite formation during mineralization. However, the XRD patterns of n-HA/COL composites exhibited a much higher intensity of the (211) plane reflection peak at about 32° (2θ) and the (222) plane peak at about 46° (2θ) than that of the other diffraction peaks characteristic to apatite, which indicated that the calcium phosphate crystals reported here were in the transition of ACP to HA crystals or in the non-classical crystallization state with a preferential growth in the (211) and (222) direction due to the influence of collagen [26].

The XRD patterns of n-HA/COL composites regulating by dual functional analogues with different aging treatments are shown in Fig. 4. When the incubation time was prolonged, the characteristic diffraction peak (002) of HA gradually emerged, but the (211) peak and the (222) peak remained significantly higher than it. This suggested that calcium
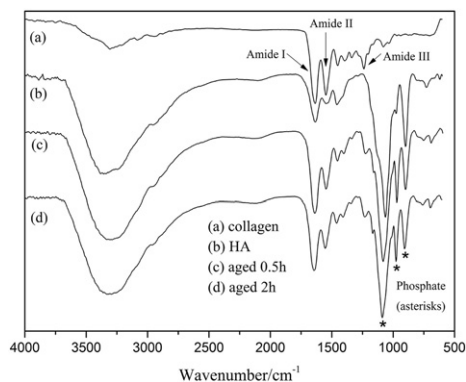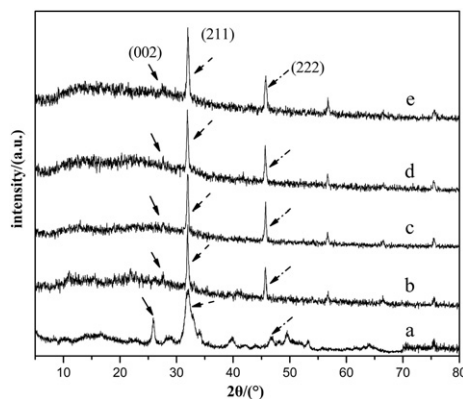

Fig. 3. XRD patterns of different control groups after aging treatment for 0.5 h at 37 °C and commercially purchased HA powder. (a) Commercial HA powder; (b) collagen negative control; (c) templating analogue control; (d) sequestration analogue control; (e) templating and sequestration analogue controls.

phosphate crystals with collagen fibrils via bottom-up nanoparticle assembly and mesocrystalline transformation were based on the non-classical crystallization approach [27,28], preferring to grow in the (211) and (222) direction.

The amount of apatite produced by the biomimetic mineralization process can be calculated using reactant. The outcome of CaCl$_2$ and β-GP used in preparing 10 mL reaction mixtures was found to be 0.048 g, and the amount of collagen used was 0.05 g, so the organic/inorganic ratio of the composite scaffold was close to 1:1.

3.3. Morphological observation of the composite scaffolds

The morphology of collagen fibrils and mineral crystals in different control groups after aging treatment for 0.5 h at 37 °C are shown in Fig. 5. It was clearly observed that the interwoven and coalescing collagen fibrils were surrounded by plenty of spherulitic or plate-like calcium phosphate crystals with crystallite size ranging between 100 nm and 200 nm in biomimetic analogue control groups. The apatite crystals produced were smaller than those in the collagen negative control. Fig. 5a showed that, in the absence of dual functional analogues, the calcium phosphate particles precipitated in collagen fibrils with an irregular shape, and some of them attempted to aggregate together. After regulation with TPP alone, numerous plate-like and spherulitic crystals were observed on the surface of collagen fibrils in Fig. 5b, which primarily showed the extrafibrillar mineralization around collagen fibrils. This phenomenon was attributed to the lack of PAA in initial process of mineralization, which could work as sequestration to stabilize amorphous
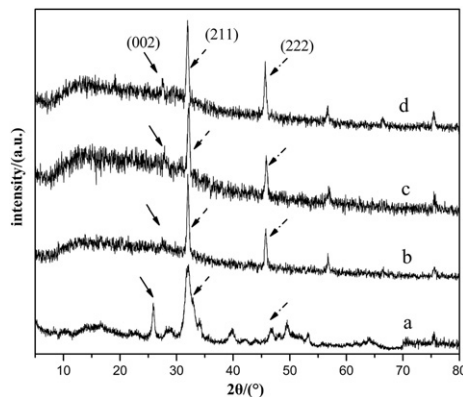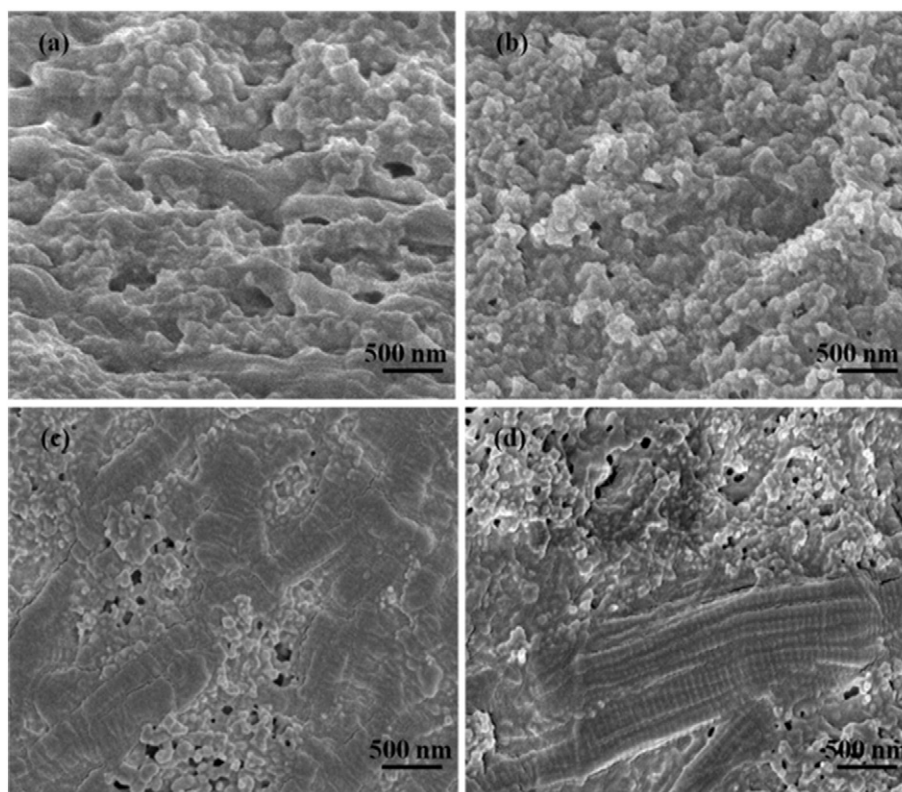

Fig. 2. FTIR spectra of collagen, synthetic hydroxyapatite and n-HA/collagen composite scaffolds subjected to different aging treatments.

Fig. 4. XRD patterns of n-HA/COL composites regulating by dual functional analogues with different aging treatments. (a) Commercial HA powder; (b) aged 0.5 h; (c) aged 2 h; (d) aged 24 h.

Fig. 5. FESEM images of collagen fibrils and mineral crystals in different control groups after aging treatment for 0.5 h at 37 °C. (a) Collagen negative control; (b) templating analogue control; (c) sequestration analogue control; (d) templating and sequestration analogues control.

calcium phosphate precursors in their required nanoscale dimensions. Without co-regulation with PAA, the ACP precursors formed were too large to penetrate into the nanoscopic gaps of collagen fibrils, which just could only precipitate randomly over the fibrillar surface and subsequently transform into spherulitic apatite crystals. Conversely, both extrafibrillar and interfibrillar mineralization could be observed in PAA-treated control groups (Fig. 5c and d). In the PAA control group (Fig. 5c), the collagen fibrils appeared swollen and had vague cross-banding patterns with plenty of plate-like apatite crystallites around them. These results indicated that because of the sequestration by PAA for ACP precursors to become stable, the collagen fibrils could be infiltrated by the smaller ACP nanophases, and hence introduced intrafibrillar mineralization. However, the self-assembled swollen fibrils had vague characteristic D-periodicity at the same time, which suggested that the ACP precursors penetrated were incapable of assembling and transforming into hierarchical apatite without TPP as a templating agent. Unlike the results shown earlier here, in the presence of dual biomimetic analogues, the collagen fibrils had apparently regular cross-banding patterns (Fig. 5d). This was attributed to the hierarchical assembly of apatite nanoplatelets directed by TPP within fibrils. More precisely, TPP was here found to simulate the templating function of phosphoproteins by attracting ACP nanoprecursors and initiating and modulating the apatite nucleation and growth within the gap zones of collagen fibril. As the free ionizable OH⁻ groups in TPP could interact with the amine groups in collagen to form ionic cross-links, with the remaining free OH⁻ groups attracting ACP precursors.

In order to obtain more detailed information about the biomimetic mineralization, HRTEM analysis of the dual biomimetic analogues control group was performed in Fig. 6. As shown in Fig. 6, the apatite nanoparticles not only precipitated on the exterior collagen fibrils (Fig. 6b), but also on the interior or at the ends (Fig. 6c and d, the short white arrows). In Fig. 6 (c and d), the long white arrows indicated the longitudinal axis of the collagen fibrils [29], and the black arrows indicated the amorphous mineral phases or crystal defects that seemed to precipitate

on the cylindrically shaped surface of fibrils [30]. The selected area electron diffraction of Fig. 6d was done to further confirm the relationship of the crystal orientation and the collagen fibrils longitudinal axis, which showed discrete arc-shaped patterns. This indicated that apatite reported was primarily in the form of nanopolycrystals, but some particles were in amorphous stages. In the SAED pattern, the arc-shaped diffractions were ascribed to (002), (211), and (222) planes of HA from the inside out, which exhibited pronounced preferential orientation of the (211) and (222) plane of HA. This was closely consistent with the results of XRD measurement.

3.4. Mechanical testing

Unconfined uniaxial compression testing and porosity measurement were performed to determine the effect of biomimetic analogues on the mechanical properties of the n-HA/COL scaffolds. As shown in Table 1, all mineralized scaffolds exhibited a reduced porosity and much higher compressive modulus than those of the pure collagen scaffolds due to the mineralization of collagen fibrils. The generated apatite resulted in reinforcement effect on scaffolds. And the templating and sequestration analogue control group showed significant improvement in mechanical properties compared to the other control groups.

Differences in the mechanical properties of n-HA/COL scaffolds in this study were mostly due to the difference of collagen fibrils mineralization among control groups, which was also consistent with the results of porosity measurement and SEM observation. In the collagen negative control group, most of the calcium phosphate particles precipitated on collagen fibrils surface were in an irregular shape, and some of them even attempted to aggregate together, which might influence the load transfer in scaffolds. In the templating analogue control group, the mineralized mineral layer on collagen fibrils surface due to the extrafibrillar mineralization resulted in the enhancement of compressive modulus and strength. With the help of PAA to work as sequestration to stabilize ACP precursors in required nanoscale dimensions, both
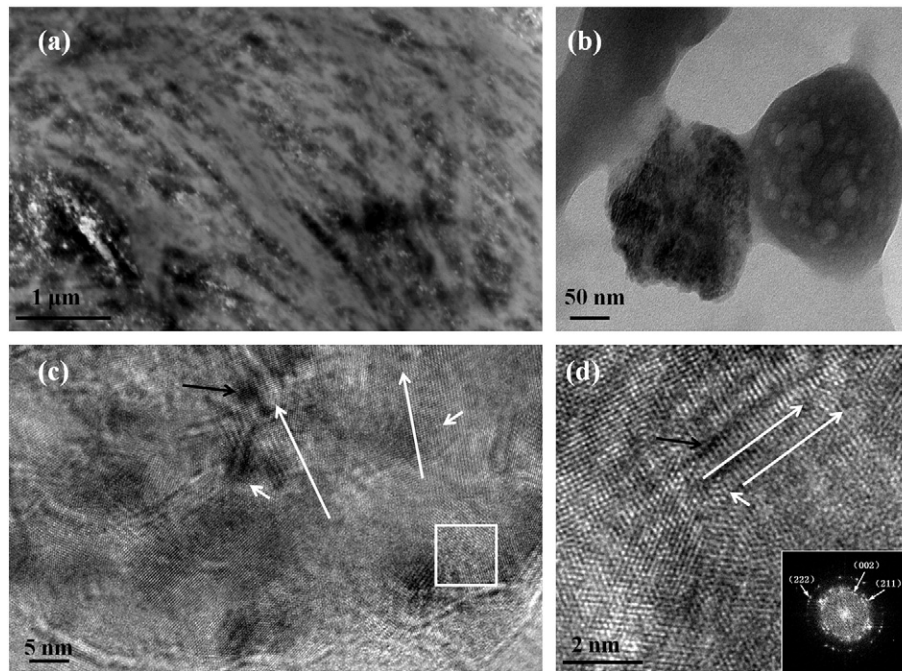
Fig. 6. TEM images of the templating-sequestration control group after aging treatment for 24 h at 37 °C. (a) TEM image of n-HA/COL composite material; (b) HRTEM image of extrafibrillar apatite precipitations; (c) HRTEM image of mineralized collagen fibrils; (d) a magnified view of the white square area in (c); inset: SAED showed discrete arc-shaped patterns. The short white arrows indicate the apatite nanoparticles precipitated on the interior or at the end of collagen fibrils; the long white arrows indicate the longitudinal axis of the collagen fibrils; the black arrows indicate the amorphous mineral phases or crystal defects.

extrafibrillar and interfibrillar mineralization could be obtained in PAA-treated control groups, which further enhanced the mechanical properties of the n-HA/COL scaffolds. However, in the sequestration analogue control, the ACP precursors penetrated were incapable of assembling and transforming into hierarchical apatite without TPP as a templating agent. Therefore, the templating and sequestration analogues control group exhibited higher compressive modulus and strength than that of the other control group due to the hierarchical assembly of apatite nanoplatelets directed by TPP within fibrils and the extrafibrillar mineral layer.

3.5. Cell adhesion

The adhesion ratio of hUCMSCs on the n-HA/COL and n-HA/COL + OICM was 89.64 ± 1.21% and 93.73 ± 1.69%, respectively. Both scaffolds showed good cell adhesion property.

SEM images (Fig. 7) showed that n-HA/COL scaffolds possessed open pores with different diameters ranging from several to about 100 μm. The cells were cultured for 7 days, after which the surfaces were almost completely covered by cells or layers of cells. On both n-HA/COL and n-HA/COL + OICM, the cells adhered to and entered the pores. The

morphology of the cells was full and each cell was attached by the secreted ECM, unlike the flat cells on the glass slide (Fig. 7d).

3.6. ALP activity

ALP enzyme activity served as a biochemical marker for examination of the differentiation of the pre-osteoblast phenotypes to the mature osteoblast phenotype [31]. Fig. 8 demonstrated that ALP expression was low on day 7, and the values for groups B, C, and D were 37.12 ± 13.12, 42.16 ± 1.47, and 32.34 ± 1.45 U/gprot, respectively, which were higher than the 22.10 ± 6.02 U/gprot for the control group. The values increased over time and the differences between the four groups were more obvious. The values for the group C were higher than those in group B with elongated culturing time, especially on day 21, showing that the n-HA/COL scaffolds benefitted the differentiation of hUCMSCs into osteoblasts. The n-HA/COL + OICM group showed the highest ALP expression, arriving to 92.21 ± 5.25 U/gprot. The value was much higher than that of the other three groups, showing that the coefficients of the n-HA/COL scaffolds and the OICM improve the expression of ALP.

Previous studies have demonstrated that natural-based polymers, such as collagen have great potential in bone tissue engineering applications. An ideal scaffold such as HA for bone regeneration should promote early mineralization and support new bone formation [32,33], so calcium phosphate bioceramics such as HA and its composites HA/COL can induce more rapid osteoblast differentiation and mineralization [34].

3.7. In vivo evaluation of bone regeneration

MRI results (Fig. 9) showed that, after 6 weeks, a slight bone defect was still visible at the implantation site of the group A, covered with bone callus. The surface was not flat, but there was no abnormal soft tissue reaction. For group B, the defect was not completely healed, showing obvious local hollowing. The bone defects in the control group showed clear gaps and edematous soft tissues. There was a clear

Table 1
The compressive modulus and compressive strength of pure collagen scaffolds and n-HA/COL composite scaffolds in different control groups after aging treatment for 24 h at 37 °C.

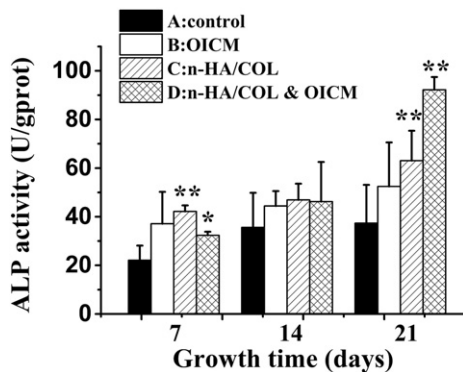| Samples	Compressive modulus (kPa)	Compressive strengths (kPa)	Porosity (%)
Pure collagen scaffolds	9.36 ± 0.86	4.12 ± 0.19	96.53 ± 0.34
Collagen negative control	26.71 ± 3.67	15.02 ± 1.93	90.90 ± 0.41
Templating analogue control	33.04 ± 0.17	21.35 ± 3.19	88.31 ± 1.76
Sequestration analogue control	45.05 ± 3.34	37.17 ± 2.60	86.42 ± 2.89
Templating and sequestration analogue controls	101.49 ± 11.39	64.07 ± 4.02	81.98 ± 2.38
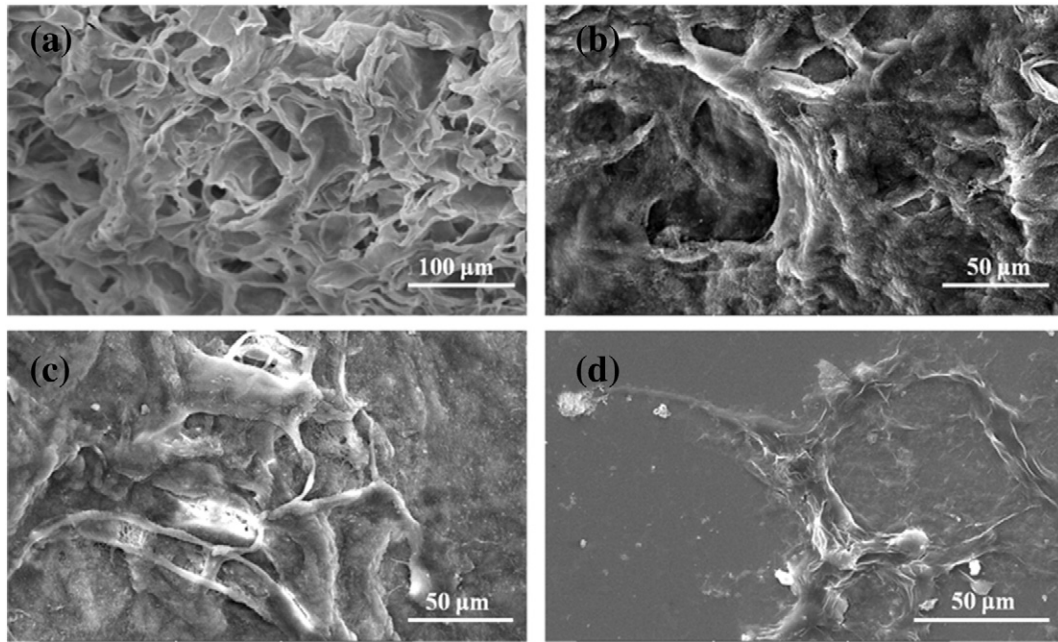
Fig. 7. SEM images of scaffolds and hUCMSCs. (a) Surface morphology of n-HA/COL materials; morphology of hUCMSCs on n-HA/COL (b), on n-HA/COL + OICM (c) and on glass slide (d) after 7 days of cell culture.

boundary between the defect and the normal bone tissues, which was filled with a small amount of crawling granulation.

After 12 weeks, the bone defects in group A were totally repaired, showing smooth and continuous periosteum. The newly formed bone was smooth to the naked eye and hard to the touch. Its morphology was similar to that of the normal femur, reaching the standard of clinical bone healing. For group B, the defects were almost healed but showed uneven formation of periosteum and callus. The bone defect site in the control group was still unfilled although the areas were reduced in size. The connection between bone and surrounding soft tissue was not complete, and the periosteal area was not smooth.
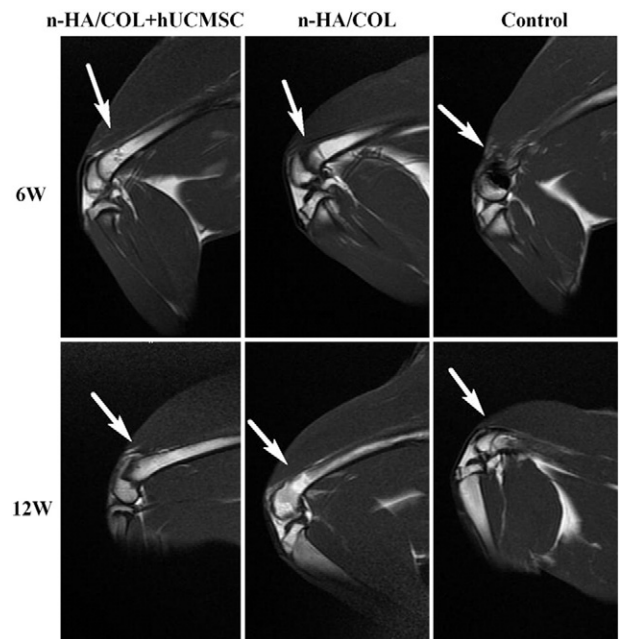
Fig. 10 shows the 3D CT images of the defects 12 weeks after implantation. The surface of the defects in group A became smoother and more integral, with no obvious dents, showing good continuity of cortical bone, which indicated the basic healing of bone defects. Group B demonstrated continuous bone and slight dent, suggesting the defect area was not completely healed, which were in accord with the Fig. 9. The defects in the control group showed obvious hollow caving and discontinuous cortical bone.

Because the HA/COL scaffold can induce more rapid osteoblast differentiation and mineralization (ALP results, Fig. 8), it will have an induction effect in non-induced cells or stem cells, and therefore increase the amount of bone formation at the periphery of defects.

New bone formation could be due to invasion of reparative cells from adjacent host tissues [33]. The images supported the enhanced bone ingrowth in scaffolds cultured with hUCMSCs. The images of MIR and CT for n-HA/COL/hUCMSCs clearly showed an almost complete healing of the defects in 12 weeks, therefore the selected implantation times seemed adequate for assessing the complete bone healing at the defected site. It should also be noted that the growing speed and density of new bones were highest in the hUCMSCs group, especially at the early healing stage, for example at the 6th week. In addition, the defects in the experiment were Ø8 mm × 6 mm, the healing effects of hUCMSCs should be more obvious in larger defects. It was concluded that the stem cells loaded in scaffolds were able to induce bone regeneration and ingrowth rapidly and effectively.

Fig. 8. The ALP activity of the cells on the n-HA/COL scaffolds and OICM after 7, 14, and 21 days. Comparison of B, C, and D to A: *$P < 0.05$; **$P < 0.01$.

Fig. 9. The MRI images of new bone formation at 6 and 12 weeks after surgery. Three groups were compared: n-HA/COL containing hUCMSC, n-HA/COL and control.
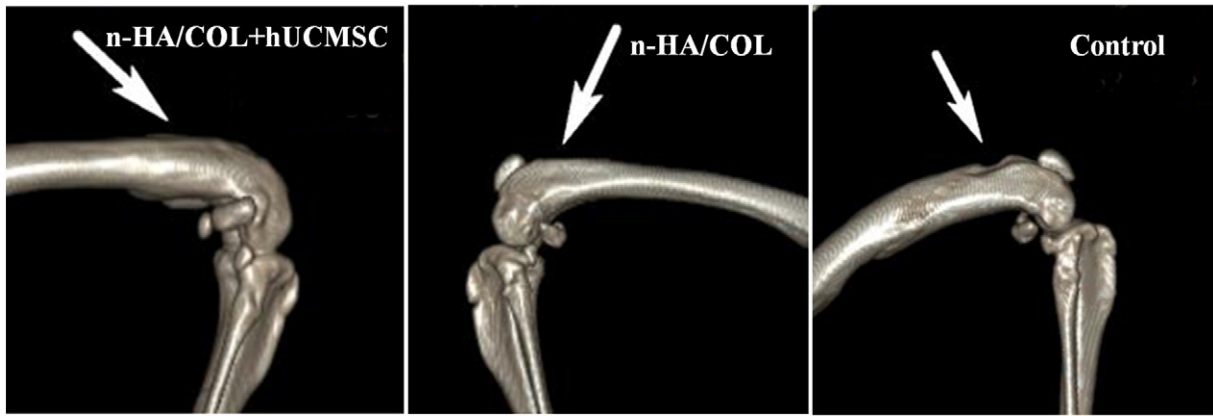
Fig. 10. The 3D CT images 12 weeks after the operation.

From histological observation, as shown in Fig. 11. Six weeks after implantation, there was a large number of osteoblasts and newly generated bones in the group A. However, the scaffolds were not completely degraded, and there were still hyperplasia of fibrous tissues at the material interface. After 12 weeks, the materials were completely absorbed and the fibrous layers were mostly disappeared. The new tissues in the area of the defect possessed more regular lamellar bone-like structure and the newly developed "Haversian" system was similar to that of the normal bone tissues. There were detectable amounts of erythrocyte indicating the growth of capillary vessels. The osteoclasts in the lamellar bone-like structure were involved in the reconstruction process. Group B demonstrated amounts of osteoid island, neutrophils, and multinucleated giant cells at the 6th week, but fibrous tissues disappeared and the materials had been completely absorbed after 12 weeks. The newly generated lamellar bone and capillary vessels were observed, similar to results observed in the normal tissue. The histological slice of the control group showed that, 6 weeks after implantation, the cells and a small amount of new bone tissue were disordered, and only a few osteoid islands were visible. Fibroblasts, neutrophils, macrophages, and other inflammatory cells were scattered among the implants. After 12 weeks, small amounts of lamellar bone tissue had formed, and muscle tissue had grown in, but there was still fibrous tissue in the defect, showing poor bone healing. The results also reveal that newly-formed bone was much thicker and more regular in the n-HA/COL + hUCMSC group than in the other two groups, regardless of 6 weeks or 12 weeks.

By animal implantation, no samples showed any marked inflammatory reactions caused by materials or cells. The scaffolds were degraded and absorbed with the formation and maturation of new bones, showing good histocompatibility of both of the hUCMSCs and mineralized materials. The results given above also indicate that the n-HA/COL scaffolds could facilitate the repair of defects and bone regeneration more efficiently than in the control group. Furthermore, the healing effects of combination of stem cells and scaffolds were higher than those of pure materials.

4. Conclusions

In this study, the intrafibrillar and extrafibrillar hydroxyapatite minerals with collagen fibrils were rapidly obtained in the presence of PAA
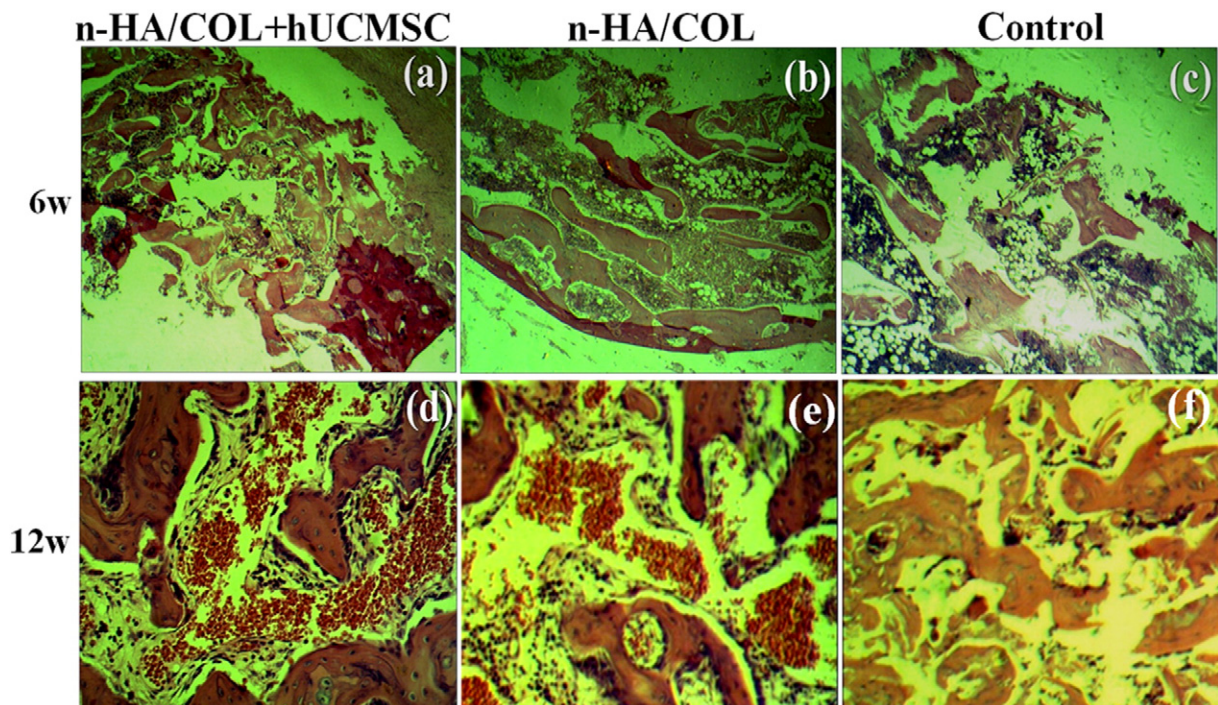

Fig. 11. Representative photomicrographs of histological analysis for the effect of the scaffolds on new bone formation at 6 and 12 weeks after surgery. Magnification for (a)–(c): 40×; (d)–(f): 200×.

and TPP as biomimetic functional analogues, facilitating co-assembly of mineral phases and collagen fibrils. The heavily mineralized n-HA/COL scaffolds promoted adhesion, proliferation, and differentiation of hUCMSCs. Most important of all, the experiment showed very positive results regarding the feasibility of hUCMSCs for in-situ bone formation in immune animals, and the combination of scaffolds/hUCMSCs served as an effective method of facilitating the healing of non-load-bearing bone defects.

Acknowledgements

References

[1] Y. Li, A. Asadi, M.R. Monroe, E.P. Douglas, pH effects on collagen fibrillogenesis in vitro: electrostatic interactions and phosphate binding, Mater. Sci. Eng. C 29 (2009) 1643–1649.
[2] J.P.R.O. Orgel, A. Miller, T.C. Irving, R.F. Fischetti, A.P. Hammersley, T.J. Wess, The in situ supermolecular structure of type I collagen, Structure 9 (2001) 1061–1069.
[3] J.P.R.O. Orgel, T.C. Irving, A. Miller, T.J. Wess, Microfibrillar structure of type I collagen in situ, Proc. Natl. Acad. Sci. U. S. A. 103 (2006) 9001–9005.
[4] Y. Wang, T. Azaïs, M. Robin, A. Vallée, C. Catania, P. Legriel, G. Pehau-Arnaudet, F. Babonneau, M.-M. Giraud-Guille, N. Nassif, The predominant role of collagen in the nucleation, growth, structure and orientation of bone apatite, Nat. Mater. 11 (2012) 724–733.
[5] F.H. Silver, W.J. Landis, Deposition of apatite in mineralizing vertebrate extracellular matrices: a model of possible nucleation sites on type I collagen, Connect. Tissue Res. 52 (2011) 242–254.
[6] M.J. Olszta, X. Cheng, S.S. Jee, R. Kumar, Y.-Y. Kim, M.J. Kaufman, E.P. Douglas, L.B. Gower, Bone structure and formation: a new perspective, Mater. Sci. Eng. R. Rep. 58 (2007) 77–116.
[7] F. Nudelman, K. Pieterse, A. George, P.H.H. Bomans, H. Friedrich, L.J. Brylka, P.A.J. Hilbers, G. de With, N.A.J.M. Sommerdijk, The role of collagen in bone apatite formation in the presence of hydroxyapatite nucleation inhibitors, Nat. Mater. 9 (2010) 1004–1009.
[8] A. George, A. Veis, Phosphorylated proteins and control over apatite nucleation, crystal growth, and inhibition, Chem. Rev. 108 (2008) 4670–4693.
[9] A.S. Deshpande, E. Beniash, Bio-inspired synthesis of mineralized collagen fibrils, Cryst. Growth Des. 8 (2008) 3084–3090.
[10] G.K. Hunter, J. O'Young, B. Grohe, M. Karttunen, H.A. Goldberg, The flexible polyelectrolyte hypothesis of protein–biomineral interaction, Langmuir 26 (2010) 18639–18646.
[11] Y. Liu, Y.-K. Kim, L. Dai, N. Li, S.O. Khan, D.H. Pashley, F.R. Tay, Hierarchical and non-hierarchical mineralisation of collagen, Biomaterials 32 (2011) 1291–1300.
[12] F. Nudelman, A.J. Lausch, N.A.J.M. Sommerdijk, E.D. Sone, In vitro models of collagen biomineralization, J. Struct. Biol. 183 (2013) 258–269.
[13] W. Chen, J. Liu, N. Manuchehrabadi, M.D. Weir, Z. Zhu, H.H.K. Xu, Umbilical cord and bone marrow mesenchymal stem cell seeding on macroporous calcium phosphate for bone regeneration in rat cranial defects, Biomaterials 34 (2013) 9917–9925.
[14] N. Roveri, G. Falini, M.C. Sidoti, A. Tampieri, E. Landi, M. Sandri, B. Parma, Biologically inspired growth of hydroxyapatite nanocrystals inside self-assembled collagen fibers, Mater. Sci. Eng. C 23 (2003) 441–446.
[15] L. Zhao, E.F. Burguera, H.H.K. Xu, N. Amin, H. Ryou, D.D. Arola, Fatigue and human umbilical cord stem cell seeding characteristics of calcium phosphate–chitosan–biodegradable fiber scaffolds, Biomaterials 31 (2010) 840–847.
[16] A. Can, S. Karahuseyinoglu, Concise review: human umbilical cord Stroma with regard to the source of fetus-derived stem cells, Stem Cells 25 (2007) 2886–2895.
[17] Y. Diao, Q. Ma, F. Cui, Y. Zhong, Human umbilical cord mesenchymal stem cells: osteogenesis in vivo as seed cells for bone tissue engineering, J. Biomed. Mater. Res. Part A 91A (2009) 123–131.
[18] C. Rosada, J. Justesen, D. Melsvik, P. Ebbesen, M. Kassem, The human umbilical cord blood: a potential source for osteoblast progenitor cells, Calcif. Tissue Int. 72 (2003) 135–142.
[19] A. Sionkowska, J. Kozłowska, Properties and modification of porous 3-D collagen/hydroxyapatite composites, Int. J. Biol. Macromol. 52 (2013) 250–259.
[20] K.E. Mitchell, M.L. Weiss, B.M. Mitchell, P. Martin, D. Davis, L. Morales, B. Helwig, M. Beerenstrauch, K. Abou-Easa, T. Hildreth, D. Troyer, Matrix cells from Wharton's jelly form neurons and glia, Stem Cells 21 (2003) 50–60.
[21] M. Zhao, L. Li, X. Li, C. Zhou, B. Li, Three-dimensional honeycomb-patterned chitosan/poly(ʟ-lactic acid) scaffolds with improved mechanical and cell compatibility, J. Biomed. Mater. Res. Part A 98A (2011) 434–441.
[22] L. Xu, A.L. Anderson, Q. Lu, J. Wang, Role of fibrillar structure of collagenous carrier in bone sialoprotein-mediated matrix mineralization and osteoblast differentiation, Biomaterials 28 (2007) 750–761.
[23] Y. Arai, D.L. Sparks, ATR–FTIR spectroscopic investigation on phosphate adsorption mechanisms at the ferrihydrite–water interface, J. Colloid Interface Sci. 241 (2001) 317–326.
[24] M. Jackson, L.-P.i. Choo, P.H. Watson, W.C. Halliday, H.H. Mantsch, Beware of connective tissue proteins: assignment and implications of collagen absorptions in infrared spectra of human tissues, Biochim. Biophys. Acta (BBA) - Mol. Basis Dis. 1270 (1995) 1–6.
[25] Y. Zhai, F.Z. Cui, Y. Wang, Formation of nano-hydroxyapatite on recombinant human-like collagen fibrils, Curr. Appl. Phys. 5 (2005) 429–432.
[26] A. Ficai, E. Andronescu, G. Voicu, C. Ghitulica, B.S. Vasile, D. Ficai, V. Trandafir, Self-assembled collagen/hydroxyapatite composite materials, Chem. Eng. J. 160 (2010) 794–800.
[27] M. Niederberger, H. Colfen, Oriented attachment and mesocrystals: non-classical crystallization mechanisms based on nanoparticle assembly, Phys. Chem. Chem. Phys. 8 (2006) 3271–3287.
[28] T.-S. Wong, B. Brough, C.-M. Ho, Creation of functional micro/nano systems through top-down and bottom-up approaches, Mol. Cell. Biomech. 6 (2009) 1–55.
[29] X.J. Yang, C.Y. Liang, Y.L. Cai, K. Hu, Q. Wei, Z.D. Cui, Recombinant human-like collagen modulated the growth of nano-hydroxyapatite on NiTi alloy, Mater. Sci. Eng. C 29 (2009) 25–28.
[30] Y. Zhai, F.Z. Cui, Recombinant human-like collagen directed growth of hydroxyapatite nanocrystals, J. Cryst. Growth 291 (2006) 202–206.
[31] L.H. Li, K.P. Kommareddy, C. Pilz, C.R. Zhou, P. Fratzl, I. Manjubala, In vitro bioactivity of bioresorbable porous polymeric scaffolds incorporating hydroxyapatite microspheres, Acta Biomater. 6 (2010) 2525–2531.
[32] L. Xiaoming, F. Yubo, W. Fumio, Current investigations into carbon nanotubes for biomedical application, Biomed. Mater. 5 (2010) 022001.
[33] E. Biazar, S. Heidari Keshel, M. Rezaei Tavirani, R. Jahandideh, Bone formation in calvarial defects by injectable nanoparticular scaffold loaded with stem cells, Expert. Opin. Biol. Ther. 13 (2013) 1653–1662.
[34] H.J. Lee, J.K. Lee, H. Lee, J.E. Carter, J.W. Chang, W. Oh, Y.S. Yang, J.-G. Suh, B.-H. Lee, H.K. Jin, J.-s. Bae, Human umbilical cord blood-derived mesenchymal stem cells improve neuropathology and cognitive impairment in an Alzheimer's disease mouse model through modulation of neuroinflammation, Neurobiol. Aging 33 (2012) 588–602.